RESEARCH ARTICLE

Contribution of mean and eddy momentum processes to tropical cyclone intensification

Michael T. Montgomery[1] | Gerard Kilroy[2] | Roger K. Smith[2] | Nina Črnivec[2]

[1]Department of Meteorology, Naval Postgraduate School, Monterey, California

[2]Meteorological Institute, Ludwig-Maximilians University of Munich, Munich, Germany

Correspondence
Michael T. Montgomery, Department of Meteorology, Naval Postgraduate School, Monterey, CA, USA.
Email: mtmontgo@nps.edu

Funding information
Deutsche Forschungsgemeinschaft, Grant/Award Number: KI-2248; National Science Foundation, Grant/Award Numbers: IAA-1656075, AGS-1313948; Office of Naval Research, Grant/Award Number: N0001417WX00336

Abstract

An idealized, three-dimensional, 1 km horizontal grid spacing numerical simulation of a rapidly intensifying tropical cyclone is used to extend basic knowledge on the role of mean and eddy momentum transfer on the dynamics of the intensification process. Examination of terms in the tangential and radial velocity tendency equations provides an improved quantitative understanding of the dynamics of the spin-up process within the inner-core boundary layer and eyewall regions of the system-scale vortex. Unbalanced and non-axisymmetric processes are prominent features of the rapid spin-up process. In particular, the wind asymmetries, associated in part with the asymmetric deep convection, make a substantive contribution ($\sim$30%) to the maximum wind speed inside the radius of this maximum. The analysis provides a novel explanation for inflow jets sandwiching the upper-tropospheric outflow layer which are frequently found in numerical model simulations. In addition, it provides an opportunity to assess the applicability of generalized Ekman balance during rapid vortex spin-up. The maximum tangential wind occurs within and near the top of the frictional inflow layer and as much as 10 km inside the maximum gradient wind. Spin-up in the friction layer is accompanied by supergradient winds that exceed the gradient wind by up to 20%. Overall, the results affirm prior work pointing to significant limitations of a purely axisymmetric balance description, for example, gradient balance/Ekman balance, when applied to a rapidly intensifying tropical cyclone.

KEYWORDS
boundary layer, hurricane, tropical cyclone, typhoon, vortex intensification

1 | INTRODUCTION

The problem of understanding tropical cyclone intensity change has been at the cutting edge of meteorological research in recent years, especially in the context of the rapid intensification or rapid decay of storms threatening landfall in populated coastal communities. This is because of the continued challenges in forecasting intensity change, a phenomenon which involves processes with scales spanning many orders of magnitude.

Most of the available paradigms for understanding tropical cyclone intensification are based, for simplicity, on axisymmetric models and most have considered the prototype problem, which addresses the evolution of an

initially cloud-free, warm-cored, symmetric vortex in gradient wind and hydrostatic balance in a quiescent environment on an f-plane. However, such models have been shown to have inherent limitations for understanding the intensification process because they represent convection in the form of axisymmetric rings (Persing *et al.*, 2013).

As shown in many previous studies, for much of the intensification phase of a simulated storm, the flow is markedly asymmetric (Montgomery *et al.*, 2006; Nguyen *et al.*, 2008; Fang and Zhang 2011; Persing *et al.*, 2013; Kilroy *et al.*, 2016, 2017, 2018). This is because deep convective structures, which are a key component of the intensification process, are intrinsically three-dimensional and their locations within the vortex have a stochastic element. In fact, the azimuthally averaged fields of, for example, vertical velocity, vertical vorticity, diabatic heating rate and regions of saturation are *dominated* by such structures. Accordingly, eddy processes and the accompanying asymmetric vortex waves must be an integral part of a complete dynamical explanation of the vortex behaviour.

For the foregoing reasons, a paradigm for tropical cyclone intensification that incorporates the three-dimensional nature of deep convection has been developed over the last decade or more, the so-called *rotating-convection paradigm*. The rotating-convection paradigm is reviewed by Smith and Montgomery (2016) and Montgomery and Smith (2014, 2017) in the context of the prototype problem. While the main focus of the rotating-convection paradigm has been on the dynamical mechanisms involved in the spin-up process, the paradigm acknowledges the need for a modest elevation of surface enthalpy fluxes to sustain the deep convection required for vortex spin-up. On the dynamical side, it has been recognized for some time that the intensification of a realistic tropical cyclone involves marked deviations from classical axisymmetric balance dynamics, which assumes a slow evolution of an axisymmetric vortex in strict gradient and hydrostatic balance subject to forcing by heat release and tangential momentum sources or sinks. Such deviations were highlighted by a high-resolution (at that time, horizontal grid spacing 6 km) simulation of hurricane *Andrew* (1992) by Zhang *et al.* (2001). These authors set out, *inter alia*, to answer three main questions (p. 93): "To what extent is the gradient wind balance model a good approximation to the local and azimuthally averaged tangential winds in an intensifying hurricane? What causes the gradient wind imbalance locally and in an azimuthally averaged state? What is the intensifying mechanism of tangential winds in the eyewall?"

Their answer to the first question was yes, to a degree within approximately 10%. However, supergradient winds were found to be an important feature of the corner flow region of the simulated storm and also in the eyewall where the air motion has an outward component. Zhang *et al.* (2011, p. 106) explained the development of the supergradient wind and spin-up of the eyewall as follows: "As the storm deepens, the cross-isobaric radial inflow in the marine boundary layer transports more absolute angular momentum from the hurricane environment into the eyewall region than frictional dissipation. The major radial inflow decelerates as it approaches the radius of maximum wind where the centrifugal force exceeds radial pressure gradient force. … Then, all the inflow air mass must ascend in the eyewall, transporting absolute angular momentum upward to spin up the tangential flow above. This upward transport of absolute angular momentum could increase significantly the local centrifugal force, thereby causing the pronounced supergradient acceleration and the development of radial outflow in the eyewall. In the present case, the supergradient acceleration occurs at the same order of magnitude as radial pressure gradient force in the vicinity of V_{max} (the maximum wind speed, our insertion), and accounts for the generation of an outflow jet near the top of the marine boundary layer. However, the local changes in tangential winds are always small due to the intense advection in the eyewall. It is evident that (a) the intensity of the radial outflow depends critically on the upward transport of absolute angular momentum, and (b) the spin-down of the eyewall by radial outflow must be overcompensated by the upward transport of absolute angular momentum if the storm is to deepen. Of course, the underlying ocean (and latent heat release in the eyewall) is the fundamental energy source for the deepening of tropical cyclones."

According to the above view, the evaporation of water from the underlying ocean supports a nonlinear spin-up process wherein the development of supergradient winds in the boundary layer of the vortex, in combination with the upward transport of absolute angular momentum from the boundary layer, play an important role in the intensification of the storm's eyewall cloud. Similar findings were reported in idealized, but finer resolution numerical simulations by Smith *et al.* (2009) and Persing *et al.* (2013). In particular, Persing *et al.* showed that the spin-up of the eyewall in the lower troposphere was accomplished primarily by resolved vertical eddy momentum fluxes in their three-dimensional configuration (Persing *et al.*, 2013, their figures 10d,g,h). The nonlinear dynamics of the vortex boundary layer and its contribution to spinning up the eyewall was discussed further from the perspective of the newly developed rotating-convection paradigm by Montgomery and Smith (2017). The upshot of the foregoing findings is that, if unbalanced and eddy processes play a marked role in spinning up a tropical cyclone eyewall,

a more complete understanding of the dynamics of the tropical cyclone boundary layer and interior is certainly warranted.

The previous work of Persing *et al.* used a 3 km horizontal grid spacing, arguably only marginally adequate for representing deep convective processes, but a question remains as to whether the convective eddy momentum fluxes were under-represented by this resolution. To address this question, we employ here a horizontal grid spacing of 1 km so as to better represent the convective eddy momentum transports. Although the Persing *et al.* study did calculate and interpret the contribution from the convective vertical transport of radial momentum, it stopped short of a complete analysis of the radial momentum equation. One application of such an analysis would be an assessment of the integrity of a balance representation of the intensification process. We address this issue here by employing an azimuthally averaged analysis of the radial momentum equation.

A recent articulation of tropical cyclone intensification by Emanuel (2018, p. 15.15) highlights the critical role of Ekman layer dynamics in the frontogenesis of the developing eyewall (in terms of equivalent potential temperature): "... the boundary layer near the radius of maximum winds is strongly frontogenetical, with convergence of the Ekman boundary layer flow guaranteed by the large radially inward increase of inertial stability as the vorticity rapidly increases inward." Given the prominence ascribed to the Ekman layer, which is only valid when the radial and vertical advection of radial momentum are negligible, a natural question arises concerning the validity of the Ekman model in a rapidly intensifying tropical cyclone. Our analysis of the radial momentum equation permits an investigation of this question, and related questions concerning the upper-level outflow and inflow-layer dynamics.

In the present study we use an idealized modeling configuration to investigate further the salient dynamical features of the boundary layer and vortex interior during the rapid intensification of the vortex. We examine also hitherto unexplored features of the flow in the upper troposphere. In particular, we aim to

a. quantify the relative contributions of the mean and eddy covariance terms to the tangential and radial accelerations in the vortex core region (including the departure from gradient wind balance), extending the work of Zhang *et al.* (2001) and Persing *et al.* (2013);
b. assess the validity of generalized Ekman balance (Abarca *et al.*, 2015; Smith and Montgomery, 2020) in the inner-core boundary layer during rapid intensification; and

c. investigate and offer an explanation for inflow jets sandwiching the upper-tropospheric outflow layer, structures which are frequently found in numerical model simulations (e.g., figures 15a, 17a of Persing *et al.*, 2013; figure 2 of Ohno and Satoh, 2015; figure 2 of Kilroy *et al.*, 2018; figure 2b,d of Smith *et al.*, 2018). These inflow structures develop as part of the intensification process and, as they contribute to the spin-up of tangential winds at upper levels by carrying absolute angular momentum inwards, it would seem appropriate to investigate their origin. As far as we are aware, there has been no satisfactory explanation for these upper-level inflow jets.

The remaining paper is organized as follows. The numerical model used and an overview of the numerical simulation are presented in Section 2. Section 3 summarizes certain aspects of the simulated vortex evolution, including a quantitative assessment of the wind asymmetries in relation to the maximum wind speed in the boundary layer. Section 4 quantifies and interprets the role of mean and eddy processes mentioned above on the azimuthal-mean tangential and radial wind tendencies during vortex spin-up. This analysis includes an examination of the development of upper-tropospheric inflow jets and generalized Ekman balance. A summary and conclusions are presented in Section 5.

2 | THE NUMERICAL MODEL

The numerical model used for the study is version 16 of the three-dimensional, non-hydrostatic cloud model CM1 (Bryan and Fritsch, 2002). In brief, the model has prediction equations for the three components of the velocity vector, specific humidity, suspended liquid, perturbation Exner function, and perturbation density potential temperature, where perturbation quantities are defined relative to a prescribed hydrostatic basic state. For simplicity, the Kessler warm rain scheme is used in which rain has a fixed fall speed of $7 \, \mathrm{m \cdot s^{-1}}$ and ice microphysical processes and dissipative heating are not included. While it is certainly true that ice processes modify the vertical profile of latent heat release, as well as the strength of downdraughts, which, in turn, modify the kinematic and thermodynamic structure of the system scale vortex (Penny *et al.*, 2016; Kilroy *et al.*, 2018; and references therein), we believe it is essential to have a zero-order model of the basic intensification process without ice as a baseline for understanding. The calculations here are carried out for a period of 5 days with data output every 15 min.

A latitude of 20°N and a constant sea surface temperature of 27 °C are assumed. The model configuration is similar to that described in section 2 of Črnivec *et al.* (2016), except that a potentially more realistic time-scale for Newtonian relaxation to the temperature field (10 days) is applied here instead of the previous default CM1 value (12 hr) (Mapes and Zuidema, 1996).[1]

The model domain is 3,010 × 3,010 km, with 1,040 grid points in the zonal and meridional directions. The inner 600 × 600 km of the domain has a constant horizontal grid spacing of 1 km, while in the outer domain the grid spacing is stretched gradually from 1 to 10 km. There are 68 vertical levels starting at a height of 50 m and extending upwards to a height of 25 km. The vertical grid spacing is 50 m in the lowest 1 km, above which it stretches smoothly to 1200 m near the model top.

To suppress the artificial reflection of internal gravity waves from the upper boundary, a Rayleigh damping layer is added at heights above 20 km. The lateral boundaries are open radiative.

The background thermodynamic state is based on the Dunion moist tropical sounding (Dunion, 2011). This sounding has a Convective Available Potential Energy of 2104 J·kg^{-1} and a Total Precipitable Water of 51.5 kg·m^{-2}.

The values for the subgrid-scale turbulence mixing lengths are based on the recent observational findings of Zhang and Montgomery (2012) and Zhang *et al.* (2011), respectively, and the resulting vertical and horizontal eddy diffusivities output in prior model simulations of Persing *et al.* (2013). The chosen values of horizontal mixing length l_h=700 m and vertical mixing length l_v=50 m are close to the values recommended by Bryan (2012) in order to produce realistic hurricane structure. For simplicity, these mixing lengths are assumed constant in both space and time.

---

[1]The differences in results between the two simulations does not become manifest during the intensification phase, and only becomes noticeable in the maximum tangential wind during the decay phase of the simulated storm. For example, with a 10-day relaxation time-scale, there is some warming of the far field environment, especially at upper levels, after about 4–5 days of integration. This warming does not occur with the default, smaller, time-scale. We have found in our previous studies of real-life events in the European Centre for Medium Range Weather Forecasts operational analyses (not shown) that the large-scale environment surrounding tropical cyclones warms on the order of about 2–4 K over a ten-day period (as seen, for example, in averaged temperature difference plots of tropical cyclone *George* (2007) and tropical cyclone *Carlos* (2011)). These findings provide some evidence that the default time-scale for relaxation in CM1 is strongly over-relaxing to the initial sounding in the case of a mature hurricane. In any case, with a 10-day relaxation time-scale, there is not sufficient warming on the order of 5 days to strongly affect vortex evolution. In the simulation presented here, the far field warms by about 1 K between heights of 5 and 15 km over the 5-day time period integrated.

The initial vortex is axisymmetric and in thermal wind balance. The initial tangential wind speed has a maximum of 15 m·s^{-1} at the surface and at a radius of 100 km. The tangential wind speed decreases sinusoidally with height, becoming zero at a height of 20 km. Above this height, the tangential wind is set to zero.

The balanced pressure, density and temperature fields consistent with this prescribed tangential wind distribution are obtained using the method described by Smith (2006). The choice of this relatively strong initial vortex bypasses the genesis phase, which was examined in detail by e.g. Kilroy *et al.* (2017) and references therein.

# 3 | SOME ASPECTS OF VORTEX EVOLUTION

To provide a context for the analysis of mean and eddy effects, we summarize briefly the time evolution of the vortex and then present characteristics of the low-level flow field during the spin-up phase. In the diagnostic analyses presented here, we use a cylindrical polar coordinate system (r,λ,z), where r is the radius, λ is the azimuth and z is the height, and corresponding velocity components (u,v,w). The axis of coordinates is located at the surface pressure minimum[2].

3.1 | Time series of v_{max}

Figure 1 shows a time series of the maximum azimuthally-averaged tangential wind speed (v_{max}) and maximum total wind speed (vT_{max}) during the 5-day integration period. Following a brief gestation period lasting about 24 hr, the vortex begins a period of rapid intensification (RI), lasting from about 24 to 96 hr. At this time the vortex reaches its mature stage, with a maximum intensity of about 81 m·s^{-1}. The vertical lines shown in the figure highlight times for which extensive analyses will be presented later.

Significantly, vT_{max} exceeds v_{max} as soon as deep convection forms early in the gestation period. The difference between these two quantities, which is typically up to 10 m·s^{-1}, quantifies the distinction between mean tangential velocity and total wind speed, the latter of which

---

[2]The vortex centre location is obtained by finding the minimum in a filtered surface pressure field, subject to the requirement that the vortex does not move more than 20 km in a single output time. This requirement prevents the centre-finding algorithm from locking on to a localized region of strong convection. Since there is no ambient vertical shear in the problem, it is reasonable to take the centre location to be independent of height.
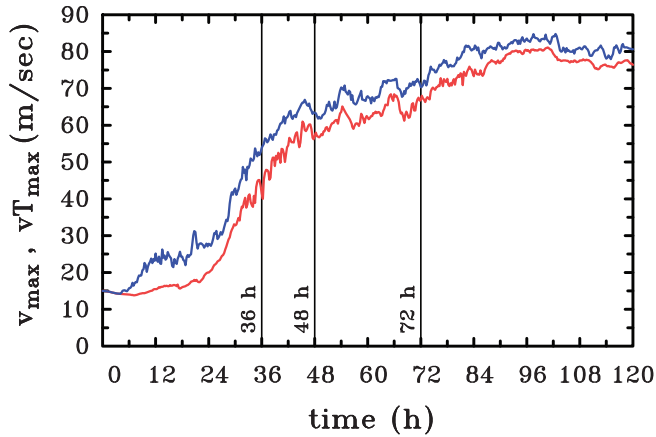
FIGURE 1   Time series of maximum azimuthally averaged tangential wind speed (v_{max}, red curve) and maximum total wind speed (vT_{max}, blue curve). The different phases of evolution discussed in the text are identified by thin vertical lines

includes the azimuthally averaged tangential velocity and radial inflow and wind eddies also. The heights of both v_{max} and vT_{max} are typically below 1 km, within the frictional boundary layer.

3.2 | Low-level radial wind profiles

We examine next the low-level wind structure in the high wind speed region of the developing vortex at selected times. This analysis will prove useful later in our interpretation of the horizontal momentum dynamics of the inner-core vortex.

Figure 2 shows radial profiles of the azimuthally averaged tangential velocity component, v, the corresponding gradient wind[3], v_{gr}, at roughly the height of the tangential wind maximum (725 m), and the similarly averaged radial velocity component, u, at the lowest model level (25 m) at 36, 48 and 72 hr during the RI phase. Shown also are the radial profiles of maximum total wind speed $vT = \max(\sqrt{u^2 + v^2})$ and maximum total eddy wind speed vTp in the lowest 1 km at each radius. The total eddy wind speed is defined as $\max(\sqrt{u'^2 + v'^2})$, where a prime denotes the difference between the total and azimuthally averaged variable.

At 36 hr, v is approximately equal to v_{gr} beyond a radius of 45 km, but there are small amplitude fluctuations of the difference. The maximum tangential wind is 41.3 m·s^{-1} and occurs at a radius, r_{vmax}, of 34 km, while the maximum gradient wind is 38.3 m·s^{-1} and occurs at a radius of 33 km. Between radii of 15 km and 45 km, v exceeds v_{gr}, that is, the

---

[3]The gradient wind, v_g, is obtained by solving the quadratic equation $(v_g^2/r) + fv_g - (1/\rho)\partial p/\partial r = 0$.
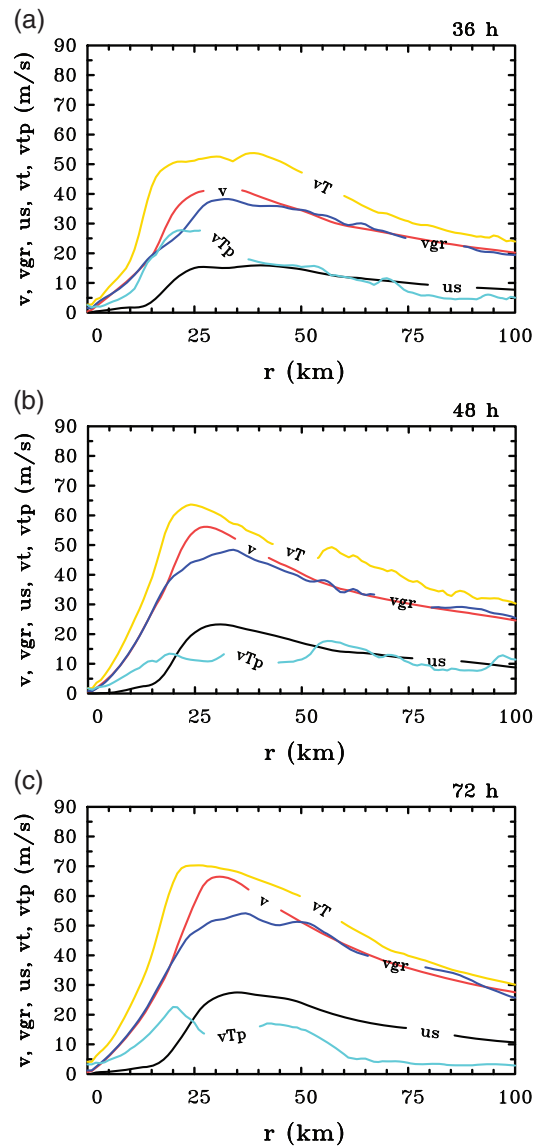
FIGURE 2   Radial profiles of azimuthally averaged tangential wind (labelled v) and gradient wind (vgr) at a height of 725 m at (a) 36 hr, (b) 48 hr and (c) 72 hr. Shown also are radial profiles of azimuthally averaged radial *inflow* (us, where s refers to the surface) at the lowest model level (25 m), the maximum total wind speed (vT) and maximum total eddy wind speed (vTp, where p refers to perturbation). The last two quantities are not spatially averaged and can occur anywhere in the lowest 1 km

tangential wind is supergradient. At r_{vmax}, v exceeds v_{gr} by 9.2%, while vT exceeds v at all radii and has its maximum at a radius outside r_{vmax}. The near-surface radial wind has a maximum of 15.9 m·s^{-1} at a radius of 41 km, the maximum being 38% of v_{max}. Notably, vTp retains a high degree of variability out to 100 km radius, suggesting that the total eddy wind speed remains a significant component of the total flow throughout the inner-core region.

At 48 and 72 hr, the results are broadly similar to the findings at 36 hr, but the velocity maxima contract

inwards with time and amplify considerably. For example, at 48 hr, v_{max} is 56.5 m·s^{-1} while the maximum gradient wind is only 47 m·s^{-1} and the near-surface maximum inflow is 22 m·s^{-1}. At this time, r_{vmax} is 26 km, while the radius of the maximum gradient wind is 34 km. Further, at r_{vmax}, the tangential wind is supergradient by 22%. The total wind speed vT exceeds the tangential wind v at all radii and, at this time, has its maximum at a radius inside r_{vmax}

At 72 hr, v_{max} is 66.5 m·s^{-1} while the maximum gradient wind is only 52 m·s^{-1} and the near-surface maximum inflow is 27.5 m·s^{-1}. At this time, r_{vmax} is 31 km (slightly outside that at 48 hr), while the radius of the maximum gradient wind is 37 km. Further, at r_{vmax}, the tangential wind is supergradient by 27.8%. Once again, vT exceeds v at all radii and, at this time, has its maximum at a radius inside r_{vmax}. As at 36 and 48 hr, the difference between vT and v and the eddy wind speed vTp profile reflect the presence of wind speed asymmetries. The total eddy wind speed remains a significant component of the total flow inside r_{vmax}. Presumably, the confinement of the maximum wind asymmetries to the region inside r_{vmax} is a reflection of the focussing of deep convection to the eyewall region of the mature vortex.

Overall, the results indicate that *the radial component of near-surface flow is a significant fraction of the tangential wind speed* and affirm the findings of Zhang *et al.* (2001) that *gradient-wind imbalance is an intrinsic feature of the boundary-layer dynamics* during vortex spin-up.

4 | ANALYSIS OF MEAN AND EDDY PROCESSES DURING VORTEX INTENSIFICATION

During intensification, multiple vortical updraughts have been shown to be a ubiquitous feature of the inner-core circulation. These updraughts act collectively to draw air parcels inwards in the low- to mid-troposphere. Above the vortex boundary layer, at least, the inflow concentrates cyclonic vorticity. These updraughts have been shown to contribute to the sign and structure of the eddy momentum fluxes in the azimuthally averaged tangential acceleration equation (Persing *et al.*, 2013). The updraughts have been shown also to excite vortex Rossby and inertia-buoyancy waves (e.g., Chen *et al.*, 2003; Reasor and Montgomery, 2015), which in turn contribute to the eddy momentum fluxes and divergence in the tangential acceleration equation. Thus, during spin-up, a complex turbulent system of rotating, deep moist convection and vortex waves comprises the eddy field of the cloudy vortex core.

A more complete understanding of the complex eddy dynamics is certainly warranted and here we take a next step in quantifying the net signatures of the updraughts and related vortex waves in the eddy terms and corresponding mean terms in the horizontal momentum equations during vortex spin-up. In particular, we extend the Persing *et al.* (2013) analysis of, *inter alia*, the mean and eddy contributions to the azimuthal-mean tangential wind tendency equation. Here we employ a higher horizontal resolution (1 km grid spacing in the inner-vortex region) and examine also the eddy and mean contributions to the corresponding radial velocity tendency equation during spin-up. The latter analysis enables one to quantify in a dynamically consistent framework:

a. the degree of gradient wind imbalance in relation to other terms in the radial acceleration equation;
b. the role of unbalanced flow processes in the spin-up of the inner-core boundary layer, the eyewall updraught complex and upper-tropospheric inflow layers; and
c. the departure from generalized Ekman balance (Abarca *et al.*, 2015; Smith and Montgomery, 2020).

4.1 | Azimuthal mean tendency equations for horizontal velocity

In a cylindrical polar coordinate system defined relative to an approximate invariant centre of circulation, the tangential and radial momentum equations may be written, respectively, as

$$\frac{\partial v}{\partial t} + u\frac{\partial v}{\partial r} + \frac{v}{r}\frac{\partial v}{\partial \lambda} + w\frac{\partial v}{\partial z} + \left(f + \frac{v}{r}\right)u = -\frac{1}{\rho r}\frac{\partial p}{\partial \lambda} + F_\lambda, \tag{1}$$

and

$$\frac{\partial u}{\partial t} + u\frac{\partial u}{\partial r} + \frac{v}{r}\frac{\partial u}{\partial \lambda} + w\frac{\partial u}{\partial z} - \frac{v^2}{r} - fv = -\frac{1}{\rho}\frac{\partial p}{\partial r} + F_r, \tag{2}$$

where (u,v,w) is the three-dimensional velocity vector (u radial, v tangential and w vertical velocities), t is the time, f is the Coriolis parameter, F_r and F_λ are the radial and tangential components of the subgrid-scale eddy-momentum flux divergence, and ρ is the density. We define an azimuthal averaging operator by the equation

$$\overline{\gamma} = \frac{1}{2\pi} \int_o^{2\pi} \gamma \, d\lambda, \tag{3}$$

and set any dependent variable γ as the sum of a mean part $\overline{\gamma}$, and an asymmetry (or eddy) γ', i.e. $\gamma = \overline{\gamma} + \gamma'$. Then, noting that, by definition, $\overline{\gamma'} = 0$, we obtain, for example, the tendency equation for the azimuthally averaged tangential

velocity:

$$
\underbrace{\frac{\partial \overline{v}}{\partial t}}_{V_t} = \underbrace{-\overline{u}(\overline{\zeta} + f)}_{V_{m\zeta}} \; \underbrace{-\overline{w}\frac{\partial \overline{v}}{\partial z}}_{V_{mv}} \; \underbrace{-\overline{u'\zeta'}}_{V_{e\zeta}} \; \underbrace{-\overline{w'\frac{\partial v'}{\partial z}}}_{V_{ev}} + \underbrace{\overline{F_\lambda}}_{V_d},
$$

(4)

where $\zeta = \overline{\zeta} + \zeta'$ is the vertical component of relative vorticity. Here, we have neglected the azimuthally averaged pressure gradient term involving perturbations of density in the azimuthal direction. As noted by Persing *et al.* (2013), this term [V_{ppg} in their equation (12)] is tiny compared with all other terms. The five terms on the right-hand side of Equation (4) are, in order: $V_{m\zeta}$ is the mean radial influx of absolute vertical vorticity; V_{mv} is the mean vertical advection of mean tangential momentum; $V_{e\zeta}$ is the eddy radial vorticity flux; V_{ev} is the vertical advection of eddy tangential momentum; and V_d is the combined mean horizontal and vertical diffusive tendency of tangential momentum, given by

$$
\underbrace{\overline{F_\lambda}}_{V_d} = \underbrace{\frac{1}{r^2 \overline{\rho}} \frac{\partial r^2 \overline{\rho} \; \overline{\tau_{r\lambda}}}{\partial r}}_{V_{dr}} + \underbrace{\frac{1}{\overline{\rho}} \frac{\partial \overline{\rho} \; \overline{\tau_{\lambda z}}}{\partial z}}_{V_{dz}},
$$

(5)

where the stress tensors (e.g., Landau and Lifshitz, 1966, p. 51) – generalized to account for anisotropic eddy momentum diffusivities) for the subgrid-scale motions – are given by

$$
\overline{\tau_{r\lambda}} = \overline{K_{m,h} \left(\frac{1}{r} \frac{\partial u}{\partial \lambda} + r \frac{\partial v/r}{\partial r} \right)},
$$

(6)

$$
\overline{\tau_{\lambda z}} = \overline{K_{m,v} \left(\frac{1}{r} \frac{\partial w}{\partial \lambda} + \frac{\partial v}{\partial z} \right)},
$$

(7)

and $K_{m,h}$ and $K_{m,v}$ are the model output horizontal and vertical momentum diffusivities, respectively.

The azimuthally averaged radial momentum equation can be written similarly as

$$
\underbrace{\frac{\partial \overline{u}}{\partial t}}_{U_t} + \underbrace{\overline{u}\frac{\partial \overline{u}}{\partial r}}_{U_{mr}} + \underbrace{\overline{\left(u'\frac{\partial u'}{\partial r} + \frac{v'}{r}\frac{\partial u'}{\partial \lambda} \right)}}_{U_{eh}} = \underbrace{-\overline{w}\frac{\partial \overline{u}}{\partial z}}_{U_{mv}} \; \underbrace{-\overline{w'\frac{\partial u'}{\partial z}}}_{U_{ev}}
$$

$$
+ \underbrace{\frac{\overline{v}^2}{r} + f\overline{v} - \frac{1}{\overline{\rho}}\frac{\partial \overline{p}}{\partial r}}_{U_{magf}} + \underbrace{\overline{\frac{v'^2}{r} - \frac{1}{\rho}\frac{\partial p'}{\partial r}}}_{U_{eagf}} + \underbrace{\overline{F_r}}_{U_d}.
$$

(8)

Here, $\overline{F_r}$ is the combined mean horizontal and vertical diffusive tendency of radial momentum, given by:

$$
\underbrace{\overline{F_r}}_{U_d} = \underbrace{\frac{1}{r\overline{\rho}}\frac{\partial r\overline{\rho}\;\overline{\tau_{rr}}}{\partial r} - \frac{\overline{\tau_{\lambda\lambda}}}{r}}_{U_{dh}} + \underbrace{\frac{1}{\overline{\rho}}\frac{\partial \overline{\rho}\;\overline{\tau_{rz}}}{\partial z}}_{U_{dz}},
$$

(9)

where the stress tensors (e.g., Landau and Lifshitz, 1966, p. 51) for the subgrid-scale motions[4] are given by

$$
\overline{\tau_{rr}} = \overline{2K_{m,h} \left(\frac{\partial u}{\partial r} \right)},
$$

(10)

$$
\overline{\tau_{\lambda\lambda}} = \overline{2K_{m,h} \left(\frac{1}{r}\frac{\partial v}{\partial \lambda} + \frac{u}{r} \right)},
$$

(11)

$$
\overline{\tau_{rz}} = \overline{K_{m,v} \left(\frac{\partial u}{\partial z} + \frac{\partial w}{\partial r} \right)}.
$$

(12)

The individual terms on the left-hand-side of Equation (8) represent: the local tendency of the mean radial velocity, U_t, the mean radial advection of radial momentum per unit mass, U_{mr}, and the mean horizontal advection of eddy radial momentum, U_{eh} per unit mass. The terms on the right-hand side of the equation are in order: U_{mv} is minus the mean vertical advection of mean radial momentum per unit mass and U_{ev} is minus the eddy vertical advection of eddy radial momentum per unit mass; U_{magf} and U_{eagf} are the mean and eddy agradient force per unit mass, respectively; and U_d is the combined mean radial and vertical diffusive tendency of radial momentum.

In contrast to the tangential momentum equation, we have chosen this pseudo-Lagrangian form of the radial momentum equation in which the left-hand side represents the material acceleration in the radial direction following the horizontal wind. Then, the sum of terms on the right-hand side can be interpreted as forces that produce pseudo-material acceleration in the radial direction. This pseudo-Lagrangian form is preferred because it facilitates a layer-wise perspective on the forces generating horizontal acceleration within the boundary layer as well as on the formation of the upper-tropospheric inflow and outflow layers. Such a choice would seem less appropriate in the tangential momentum equation as one would then lose the neat form of the radial vorticity flux term.

Note that we have chosen to write U_{magf} with $\overline{\rho}$ in the denominator. This choice requires that the azimuthal variation of ρ be retained in the definition of U_{eagf}, and assumes that $|\rho - \overline{\rho}| << \rho$, which is always well satisfied in these numerical experiments.

4.1.1 | Attributes of the mean–eddy flow partitioning

The foregoing partitioning of the flow into azimuthal mean and eddy contributions is a natural one for an

---

[4]The expression for $\overline{\tau_{rz}}$ corrects the expression given in Persing *et al.* (2013, their equation (20)) and Montgomery and Smith (2017, their equation (15)). The difference is found to be negligible.

isolated vortex, especially when applied to vortex waves (e.g., Reasor and Montgomery, 2015, and references therein). Nevertheless, care is required when interpreting the individual contributions when strong and highly azimuthally localized features punctuate the vortex flow in a particular annulus. This is because such localized features project onto both components of the partition. For example, an individual updraught within this annulus will project both into the mean and eddy components. However, the mean updraught will have a small positive value while the eddy will have a large positive value in its particular location, but a small negative value elsewhere, a consequence of the partitioning result that $\overline{w'} = 0$. The small negative value for the eddy will identically cancel the small positive value from the mean outside the region of the individual updraught.

Another issue with this partitioning is that, because the vortex centre is not exactly stationary, there may be a weak flow across the vortex axis, even in the problem studied here where the vortex environment is quiescent. Since there is no source or sink of mass at the axis, both $\bar{u}$ and $\bar{v}$ must vanish at the axis, the latter since the vorticity at the axis is finite. As a result, both mean tendency terms must be zero, implying that the sums of terms on the right-hand sides of Equations (4) and (8) must sum to zero at the axis. Because one of the terms in the expressions for U_{eh} and U_{eagf} involve v'/r, and v' may be finite at the axis, these terms must cancel. However, on a finite mesh, this cancellation may be susceptible to appreciable numerical discretization error.

Despite the foregoing cancellation issue, the formulation in terms of mean and eddy components is generally useful for providing insight as long as this attribute of the partitioning is borne in mind. As an example, the effects of eddy momentum fluxes associated with velocity perturbations due to a single updraught on the tangential-mean velocity tendency were investigated by Kilroy and Smith (2016) and a conceptual framework for the interpretation of these eddy fluxes was given.

4.2 | Tangential velocity tendency analysis

4.2.1 | Spin-up at 36 hr

Figure 3 shows radius–height plots of the 3-hr time-averaged terms in the azimuthally averaged tangential velocity tendency equation at 36 hr, which is during the period of rapid intensification (Figure 1). The time average is based on model output saved every 15 min. Figures 3a, b show the contributions to the tendency from

the mean radial vorticity flux and vertical advection, while Figures 3c, d show the corresponding eddy contributions. Figures 3e, f show the sum of the mean and eddy terms, respectively. In each panel the mean eyewall updraught is highlighted by the thick yellow contour, which shows the location of the 0.5 m·s⁻¹ vertical velocity isopleth, and the purple contours show the ±1 m·s⁻¹ radial velocity. So as to provide a spatial reference of the acceleration terms, the green curve shows the azimuthally averaged radius of maximum tangential velocity up to 16 km height.

The mean vorticity influx (Figure 3a) is large and positive in a shallow layer near the surface, marking the boundary-layer inflow region, and it is large and negative in a narrow sloping sheath just above this layer in the inner core. It is large and negative also in the eyewall updraught, extending into the upper-tropospheric outflow layer. There are a few small regions of positive vorticity flux, including a larger more coherent region in the outflow layer outside a radius of about 80 km. The principal features in the mean tendency from vertical advection (Figure 3b) are similar to those in (a), but are opposite in sign, so that there is considerable cancellation as seen in (e). This cancellation is a reflection of the fact that, above the boundary layer, absolute angular momentum is approximately conserved (appendix of Smith *et al.*, 2009).

From the perspective of the mean dynamics, the main contribution to the spin-up of the tangential wind is associated with the import of mean cyclonic absolute vorticity in the boundary layer and the vertical advection of tangential momentum so generated into the eyewall updraught. However, there is a region spanning between 1 and 3 km where the *mean* tendencies give a spin-down effect (Figure 3e). This spin-down is more than negated by the vertical eddy momentum transport discussed below.

The contributions to the mean tendency from the eddies are confined mainly to the eyewall updraught region. The eddy vorticity flux term is mostly negative (Figure 3c), but there is a region of positive tendency above about 12 km in the outflow region. The vertical advection of eddy tangential momentum (Figure 3d) is relatively large and positive below a height of 4 km, but has more of a dipole structure above this level with positive tendencies on the inner part of the eyewall updraught and negative tendencies on the outside. The combined eddy tendency in Figure 3f shows a pattern that is quite similar to the sum of the mean tendencies (Figure 3e), but of opposite sign. This tendency for cancellation is perhaps not surprising bearing in mind the attributes of the flow partitioning discussed in Section 4.1.1. Also, the combined eddy tendency in the eyewall region spanning approximately 1 to 3 km height more than compensates the spin-down effect from the combined mean terms. In essence, the vertical momentum transport

Tangential wind tendencies at 36 h
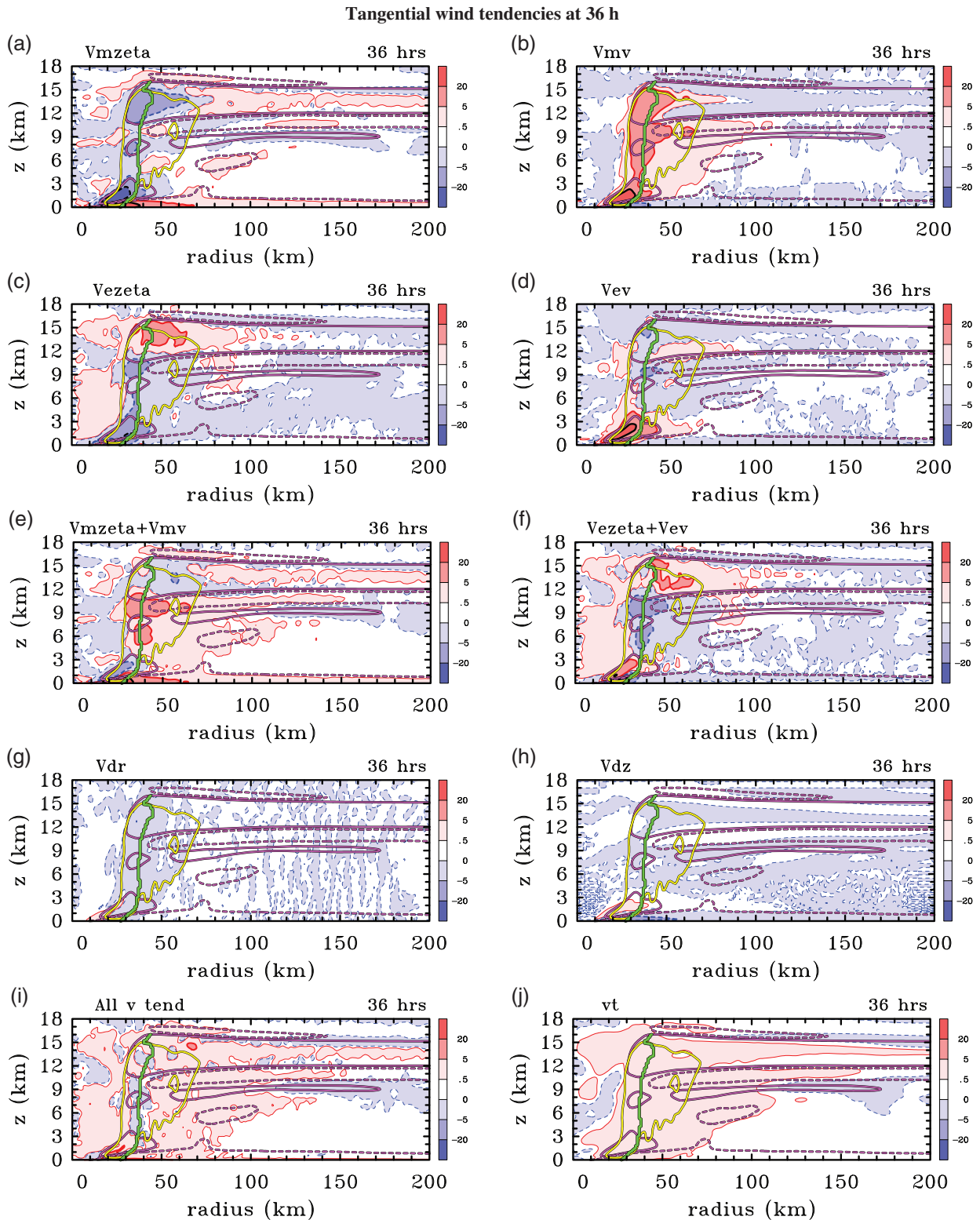
FIGURE 3 Radius–height plots of the 3 hr time-averaged terms in the azimuthally averaged tangential wind tendency equation (Equation (4)) at 36 hr. Here, Vezeta=$V_{e\zeta}$ and Vmzeta=$V_{m\zeta}$, etc. The time averaging is centred on the time shown. Shading is indicated on the side bar in m·s^{-1}·hr^{-1}, with shaded regions enclosed by contours. The thick black contour shows $\pm$ 20 m·s^{-1}·hr^{-1}. The yellow contour shows the 0.5 m·s^{-1} vertical velocity, while the purple contours show $\pm$ 1 m·s^{-1} radial velocity. The green curve shows the azimuthally averaged $r_{v\text{max}}$. Solid contours are positive, and dashed contours negative. (i) shows the sum of all tendency terms on right-hand side of Equation (4), while (j) denotes the actual mean tangential wind tendency derived from the output of the numerical simulation

in this layer is taking place principally by the convective eddy structures, affirming the findings of Persing *et al.* (2013)

The horizontal diffusive tendency shows a weak negative region in the eyewall (Figure 3g), while the vertical diffusive tendency is strongly negative in a shallow layer near the surface with a small region of positive tendency below the base of the eyewall updraught. Comparing the radial and vertical eddy terms with the corresponding subgrid-scale diffusion terms shows that the pattern of the eddy terms is generally quite different from that of the diffusion terms. The discrepancy in the pattern of tendencies implies that the resolved eddy contributions cannot be regarded simply as a down-gradient diffusive process. Persing *et al.* (2013) arrived at a similar conclusion in their study.

Comparing Figures 3a and h, one sees that the horizontal vorticity influx is generally larger than the mean vertical diffusion tendency. Even after adding the slight negative tendency from the combined eddy term near the surface, the net tendency of tangential wind (Figure 3i) is positive in the inner-core boundary layer. In essence, this is confirmation that the nonlinear boundary-layer spin-up mechanism (e.g., Smith and Montgomery, 2016) is operating to spin up the maximum tangential wind in the boundary layer. Another manifestation of this spin-up mechanism is the outward sloping region of positive values below about 4 km in height in Figure 3d. The positive values of v', which presumably contribute to the supergradient excess, are being lofted to give the positive values of V_{ev} and must be generated within the boundary layer. These positive tendency values in Figure 3d must be a result of the nonlinear boundary-layer spin-up mechanism, which acts on the asymmetric component of flow also.

The time-averaged tangential velocity tendency calculated directly from the model output is shown in Figure 3j. This tendency is simply the difference in tangential velocity over the 3 hr period divided by the 3 hr time span. The panel shows clearly that there is spin-up throughout much of the eyewall updraught, including the boundary layer beneath the eyewall and extending to approximately 60 km radius.

This direct tendency (Figure 3j) can be compared with the estimate from the sum of tendency terms (Figure 3i) on the right-hand side of Equation (4). While the direct calculation is a little smoother, the estimate does show fairly broad agreement with the direct calculation including, in particular, a sloping band of strong positive tendency, mostly inside the 0.5 m/s eyewall updraught contour. The most notable discrepancies between these two panels are found (a) in the eyewall between heights of 3 and 11 km, where there is a small region of negative tendency centred around 35 km radius, straddling the radius of maximum

wind at this time; and (b) in an outward-sloping, narrow filament at low levels (0–1.75 km, Figure 3i), approximately 5 km inside the radius of maximum wind. Possible sources for the error in the sum of tendency terms are discussed by Persing *et al.* (2013, p. 12318). In brief, there are principally three sources of error: the coarse temporal sampling of output data, the evaluation of parametrized internal diffusion and surface momentum fluxes, and the use of centred spatial differences to calculate all advection terms. (The CM1 model uses a fifth-order upwind advection scheme. The region near and inside the radius of maximum wind (RMW) is a region of high spatial gradients and our simple second-order accurate finite-difference approximation for these gradients is not expected to capture such gradients accurately.) Notwithstanding the relatively limited discrepancies within these portions of the eyewall updraught, the broad agreement elsewhere between the two calculations provides strong support to the physical interpretations of the various tendency terms given above.

4.2.2 | Later times

Similar radius–height plots to those in Figure 3 have been constructed for 48 and 72 hr (not shown), which are during the period of rapid intensification also (Figure 1). The individual tendency terms have structures that are similar to their counterparts in Figure 3, but are generally larger in magnitude on account of the quadratic nonlinearity of the momentum equations. In particular, there is still a strong mean tendency associated with the radial influx of vorticity in the boundary layer, which is partly opposed by the negative tendency due to friction. Significantly, the strong negative mean tendency $V_{m\zeta}+V_{mv}$ where the air ascends as it exits the boundary layer is opposed by a positive tendency by the sum of the eddy terms $V_{e\zeta}+V_{ev}$. This implies, again, that the eddies are playing an important role in intensifying the swirling flow in the eyewall. In the upper part of the eyewall, there is much cancellation between the sums $(V_{m\zeta}+V_{mv})$ and $(V_{e\zeta}+V_{ev})$.

4.3 | Radial velocity tendency analysis

As for the tangential momentum equation, the terms in the radial momentum equation are exemplified at 36 hr also. Radius–height plots of the 3-hr time-averaged terms in the pseudo-Lagrangian radial momentum equation at 36 h are shown in Figure 4. Selected contours of azimuthal and time-mean radial velocity are superposed on all panels to facilitate interpretation of the radial momentum dynamics. The radius of maximum azimuthally averaged

tangential velocity is superposed also for interpretation purposes.

4.3.1 | Agradient force

Figure 4a,b show the mean and eddy agradient force fields, U_{magf} and U_{eagf}, respectively. The sum of these terms represents the main driving force per unit mass for the mean radial flow. *Moreover, its departure from zero is a measure of the degree of gradient wind balance.*

As expected, U_{magf} is strongly negative in a shallow surface-based layer at radii beyond about 30 km. This negative region coincides with the frictional boundary layer in which the tangential velocity is, of course, retarded. *It is primarily this negative force field that drives the boundary-layer inflow beyond a certain radius.* Kilroy *et al.* (2016) showed that much of the low-level inflow can be attributed to boundary-layer dynamics, whereupon the "suction effect" of deep convection plays a secondary role. Near the surface, the magnitude of U_{magf} increases with decreasing radius to about 50 km and then declines rapidly. The corresponding tangential winds in this region of negative values are referred to as *subgradient*. The mean radial inflow progressively increases with decreasing radius in this layer (e.g., Figure 2a), reaching values of about $15\,\text{m}\cdot\text{s}^{-1}$, which is a significant fraction (about 38%) of the tangential winds in the same region.

Inside approximately 50 km radius and in a shallow layer that slopes upwards with radius, U_{magf} is strongly positive and serves to decelerate the inflow and even accelerate the flow outwards just above the boundary layer into the eyewall updraught. In this positive region, the tangential winds are *supergradient*. There is a negative region between heights of about 2 and 4 km. Above the negative region, U_{magf} is generally positive, being particularly strong in the inner portion of the eyewall updraught and in the outflow region to more than 100 km radius. This pattern is not surprising because air with high angular momentum is being transported vertically by deep convective cores in the developing eyewall.

The eddy agradient force field, U_{eagf} (Figure 4b) contributes to a positive radial acceleration throughout the troposphere out to between 50 and 90 km radius, where it represents an additional centrifuge effect to that of the mean term U_{magf}. In particular, U_{eagf} shows strong positive values near the surface at radii between approximately 10 and 30 km near where the surface inflow terminates, reinforcing the deceleration of the boundary-layer inflow. The relatively large values of U_{eagf} near the axis should not be taken too seriously and are presumably due to numerical inaccuracy as discussed in Section 4.1.1.

In the upper troposphere there is a region of positive U_{magf} near the top of the developing eyewall, which is thickest near the top of the eyewall and tapering to zero at a radius of about 110 km. The remainder of the upper troposphere, and, indeed, much of the lower troposphere beyond the developing eyewall updraught, has mostly negative values of U_{magf}, with magnitude not more than $5\,\text{m}\cdot\text{s}^{-1}\cdot\text{hr}^{-1}$. The subgradient tangential wind in this region acts to decelerate outflow and accelerate inflow. We will reserve further discussion on the topic of the upper-level outflow and inflow layer dynamics until Section 4.5.

4.3.2 | Other radial forces

The radius–height structure of the mean vertical advection U_{mv} in Figure 4c shows a series of layers in which U_{mv} has alternating sign. In the lowest layer, near the base of the developing eyewall updraught, $U_{\text{mv}}<0$, indicating a contribution to an increase of the radial inflow by the vertical advection of inward radial momentum from near the surface. In the sloping layer above, $U_{\text{mv}}>0$, reflecting the mean vertical transport of positive radial momentum associated with the strong outflow of air just above the boundary layer. The layer of negative U_{mv} between about 5 and 8 km height is associated with the upward transport of mean radial inflow in the eyewall updraught from the lower troposphere. The layered pattern of U_{mv} above about 8 km is consistent also with the layered pattern of inflow and outflow in the upper troposphere together with that of vertical velocity. For example, the upward transport of mean inward radial momentum from the inflow layer just below the mean outflow layer together with the downward transport of inward radial momentum from the inflow layer just above the mean outflow layer contribute to the layer of negative tendency centred at an altitude of about 12 km.

Figure 4d shows minus the eddy vertical advection of eddy radial momentum per unit mass, U_{ev}. The structure of this term, like U_{mv}, exhibits a series of layers in which U_{ev} has alternating sign. In the lower troposphere, the U_{ev} field broadly reinforces that of U_{mv}. In the upper troposphere there is a degree of cancellation between U_{mv} and U_{ev}, but the eddies can be seen to be reinforcing the strong outflow in the layer between about 11 and 14 km in height. This layer lies below the axis of the upper-level outflow layer, which implies that the eddies are acting to transport radial momentum against the mean gradient in this layer; that is, they are counter-gradient. In contrast, the layer of negative U_{ev} in the height range 14–16 km lies above the axis of the outflow layer and acts to slow down the outflow in this layer. Further, the layer of negative

Radial wind tendencies at 36 h
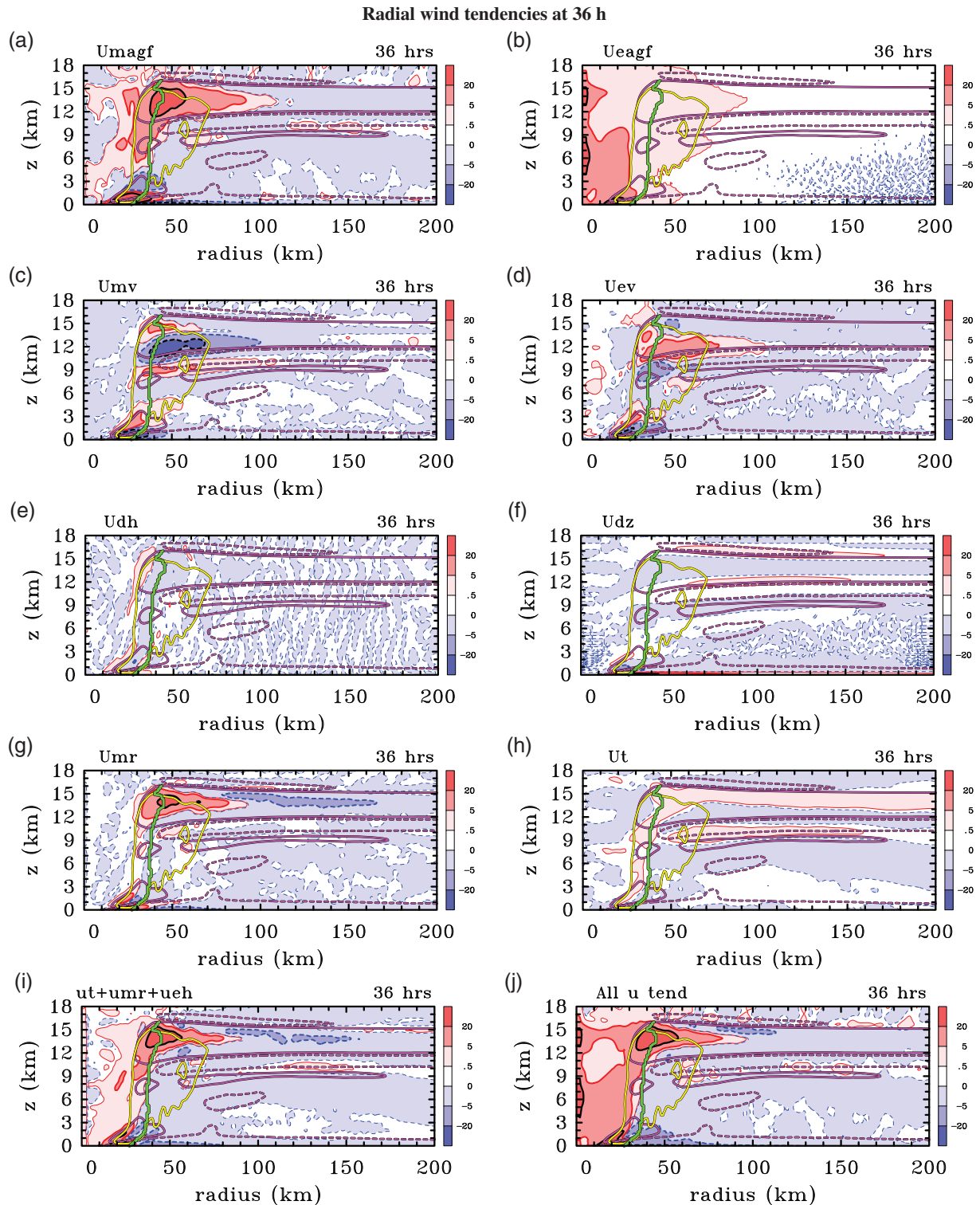
FIGURE 4 Radius–height plots of the 3-hr time-averaged terms in the azimuthally averaged radial velocity tendency equation (Equation (8)) at 36 hr. (i) shows the mean horizontal acceleration comprising the left-hand side of Equation (8); (j) shows the sum of terms on the right-hand side of Equation (8) (the forcing per unit mass); and (h) shows the temporal and azimuthal-average of the local time rate of change of mean radial velocity. The time averaging is centred on the time shown. Shading is indicated on the side bar in $m \cdot s^{-1} \cdot hr^{-1}$, with shaded regions enclosed by contours. The thick black contour shows $\pm 20 \, m \cdot s^{-1} \cdot hr^{-1}$. The yellow contour shows the $0.5 \, m \cdot s^{-1}$ vertical velocity, while the purple contours show $\pm 1 \, m \cdot s^{-1}$ radial velocity. The green curve shows the azimuthally averaged r_{vmax}. Solid contours are positive, and dashed contours negative

U_{ev} in the height range 8–11 km overlaps with the pronounced inflow layer just below the outflow layer and acts to reinforce the inflow in this layer. These features are consistent with the upper-level pattern of the vertical eddy momentum flux shown in Persing *et al.* (2013; figure 15e) and contribute to a strengthening of the primary outflow layer itself, as well as the inflow layer below the outflow layer.

Figures 4e,f show the time-averaged and azimuthally averaged subgrid-scale tendencies, U_{dh} and U_{dz}. The horizontal diffusion of radial momentum (U_{dh}) is relatively small except in the region where the radial flow terminates and turns up into the eyewall. The vertical diffusion of radial momentum (U_{dz}) shows a very shallow layer of strong positive tendency beyond a radius of about 30 km, which is a manifestation of surface friction slowing down the inflow. Above this layer lies a somewhat thicker layer of negative tendency, which is associated with the vertical diffusion of inward radial momentum through the inflow layer. This diffusion becomes particularly strong near where the boundary-layer inflow terminates.

4.3.3 | Pseudo-Lagrangian radial acceleration and net radial force

The three terms constituting the pseudo-Lagrangian radial acceleration on the left-hand side of Equation (8) consist of the local time rate of change of the mean radial flow, U_t, the horizontal mean advection of mean radial velocity, U_{mr}, and the mean of the eddy advection of eddy radial velocity, U_{eh}. All terms are time averaged over a 3-hr interval centred at 36 hr. Figure 4g,h show the structure of U_{mr} and U_t. The term U_{eh} is found to make a relatively small contribution to the total acceleration and is not shown separately.

The structure of the mean radial advection U_{mr} shows a shallow layer of elevated negative values beyond a radius of about 35 km near the surface where the flow in the boundary layer is accelerating inwards. It shows also shallow sloping regions of alternating positive and negative values, generally confined within a radius of 50 km and a height of about 3 km. The lowermost region of positive values coincides with the radii where the inflow is decelerated sharply before ascending into the eyewall.

In the upper troposphere, the radial flow accelerates outwards as the air exits the eyewall, but the region of outward acceleration is sandwiched by layers where $U_{mr} < 0$ outside a radius of about 60 km. Beyond approximately 90 km radius, the mean acceleration in the upper troposphere is inwards so that outward flowing air is

being decelerated, consistent with the pattern of U_{magf}. Moreover, inspection of the time-mean inflow (purple dash contours) during this same time interval shows that there are regions of inflow sandwiching the outflow layer and these regions overlap with that of negative U_{magf} and U_{mr}. Where this occurs, the flow in the inflow layers will be accelerated inwards.

Figure 4h shows the quantity U_t, which, if time integrated over a 3 hr interval, indicates that, over this time interval, there has been a strengthening of the radial circulation. In particular, the low-level inflow has strengthened, the outflow just above the boundary layer where the boundary layer terminates has strengthened, and the upper-level outflow has strengthened. In addition, a region of inflow being drawn in by the developing eyewall updraught in a layer between 4 and 8 km in height has strengthened.

Figure 4i shows the time-averaged pseudo-Lagrangian radial acceleration, $U_t + U_{mr} + U_{eh}$, while Figure 4j shows the corresponding net time-averaged net radial force per unit mass leading to this acceleration. These two panels encapsulate the radial momentum budget. Generally, the principal features of these two fields match each other reasonably well, despite there being a few local discrepancies in detail which are presumably associated with interpolation errors and the like (Section 4.2.1).

4.3.4 | Later times

Similar radius–height cross-sections to those in Figure 4 have been constructed at 48 and 72 hr. The tendencies in the individual panels (not shown) have structures that are similar to their counterparts in Figure 4, but, as in the case of the tangential tendency equation, the fields are generally larger in magnitude consistent with the quadratic nonlinearity of the momentum equations. As an illustrative example, Figure 5 shows the results of the mean radial velocity tendency analysis at 72 hr, a time when the system-scale vortex is approaching maximum intensity (cf. Figure 1).

Figure 5a shows the mean pseudo-Lagrangian acceleration, while Figure 5b shows the sum of the radial force per unit mass contributions. Even at this later time, there is good agreement between the structure and magnitude of the net forcing and those of the acceleration. As expected, the magnitude of radial forcing is seen to have increased considerably relative to the earlier analysis time. The increase in magnitude is particularly striking in both the lowest 2 km and in the upper troposphere between about 10 and 16 km.

Radial wind tendencies at 72 h
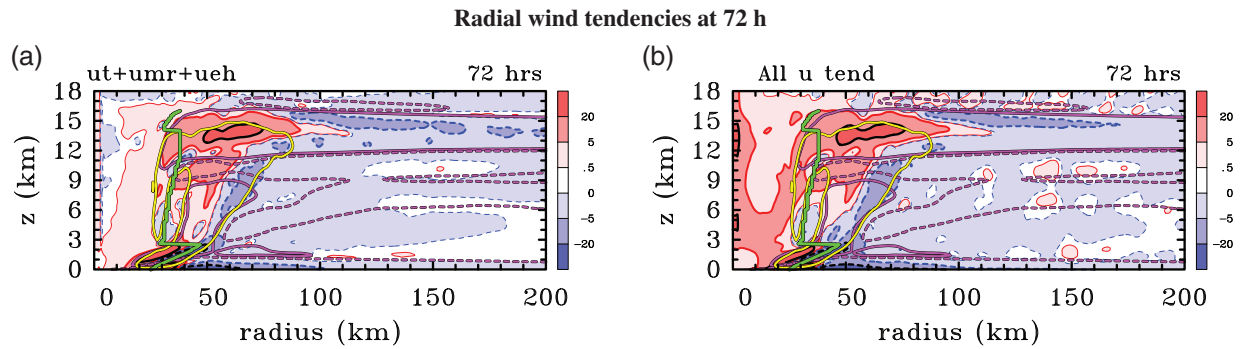
FIGURE 5 Radius–height plots of the 3 hr time-averaged terms in the azimuthally averaged radial velocity tendency Equation (8) at 72 hr. The time averaging is centred on the time shown. Shading is indicated on the side bar in $m \cdot s^{-1} \cdot hr^{-1}$, with shaded regions enclosed by contours. The thick black contour shows $\pm 20\, m \cdot s^{-1} \cdot hr^{-1}$. The yellow contour shows the $0.5\, m \cdot s^{-1}$ vertical velocity, while the pink contours show $\pm 1\, m \cdot s^{-1}$ radial velocity. The green curve shows the azimuthally averaged $r_{v\max}$. Solid contours are positive, and dashed contours are negative

4.3.5 | Summary of radial velocity analysis

Broadly speaking, there is a net inward force field through much of the lower troposphere including much of the developing eyewall region itself. This inward force is particularly strong in the inner-core boundary layer. Near the surface and just below the eyewall updraught, this time-averaged force at 36 hr exceeds $5\, m \cdot s^{-1} \cdot hr^{-1}$. Inside the developing eyewall, near its inner edge, and throughout much of the upper troposphere out to a radius of about 100 km, there is strong positive radial acceleration, exceeding $20\, m \cdot s^{-1} \cdot hr^{-1}$ in the upper troposphere. The net radial force is associated primarily with the pattern of mean agradient force and the mean and eddy vertical advection terms (Figure 5a, c, d). Similar results are found at later times, with the magnitude of the net radial force field increasing substantially as the vortex attains a mature intensity.

The flow in much of the inner-core region is significantly unbalanced in the radial direction, especially at low levels and in the upper troposphere. This finding strongly supports the results and interpretations of Zhang *et al.* (2001). Thus, while the assumption of gradient wind balance may be a defensible zero-order approximation through much of the middle troposphere during spin-up, the assumption cannot be justified in the inner-core boundary layer or in the upper troposphere in the region of strong outflow. The radial force fields demonstrate that even a generalized Ekman balance (i.e., a balance between the linearized form of U_{magf} and U_{dz}, discussed further below) is strongly violated in the inner-core boundary layer, where the terms U_{mv}, U_{ev} and U_{eagf} are comparable in magnitude to U_{magf} and cannot be meaningfully neglected in a zero-order approximation.

4.4 | Validity of generalized Ekman balance?

In recent years, generalized Ekman balance has been invoked to help explain the dynamics of the tropical cyclone boundary layer during steady-state, spin-up and secondary eyewall formation phases (e.g., Kepert, 2001; Kepert and Wang, 2001; Kepert, 2013). Like traditional Ekman balance (e.g., Gill, 1982) comprising a balance between pressure gradient, Coriolis and viscous forces in the atmospheric boundary layer, generalized Ekman balance involves a balance between pressure gradient, generalized Coriolis and viscous forces. This vortex Ekman balance, and issues concerning its interpretation for tropical cyclone vortices, are reviewed and analyzed by Smith and Montgomery (2020). In the notation of Section 4.1, the generalized Ekman balance in the radial direction takes the form:

$$0 = U_{\text{magf}} + U_{\text{dz}}, \qquad (13)$$

where U_{magf} is the agradient force defined in Section 4.1 (equal to the sum of radial pressure gradient, Coriolis and centrifugal forces), $U_{\text{dz}} = K_v \partial^2 \bar{u}/\partial z^2$ is the vertical diffusion of radial momentum and K_v the vertical momentum diffusivity (assuming for simplicity the vertical diffusivity K_v is locally constant). Although this generalized balance is comprised strictly of the linearized form of U_{magf}, we retain the un-approximated form here for simplicity. As is evident after inspecting Figure 4a,f, although this balance is reasonably satisfied in the outer vortex boundary layer, it is not at all satisfied in the inner-core boundary layer around the radius of maximum tangential wind wherein U_{dz} is small in comparison to U_{magf}. Indeed, Figure 4 shows that within approximately 70 km from the vortex centre, all terms, save for the radial diffusion, U_{dh},

contribute markedly to the radial momentum balance in the corner flow region of the rapidly developing vortex. In particular, the radial advection of mean radial velocity, U_{mr} and the vertical advection of mean radial velocity, U_{mv} make significant contributions to the radial acceleration just outside and underneath the eyewall complex. The eddy centrifugal acceleration U_{eagf} and eddy vertical advection of eddy radial velocity U_{ev} are non-negligible also in this region. These results are found to hold true at later times during the intensification process (not shown), and can be anticipated by the quadratic nonlinearity of the equations as the vortex strengthens.

A similar assessment may be conducted for the vortex Ekman balance in the tangential direction comprising a balance between the mean vorticity influx and the retardation of tangential momentum by vertical diffusion into the underlying ocean, that is,

$$0 = V_{m\zeta} + V_{dz}, \qquad (14)$$

where $V_{m\zeta}$ is the mean vorticity influx as defined in Section 4, and $V_{dz} = K_v \partial^2 \bar{v}/\partial z^2$ is the vertical diffusion of tangential momentum (assuming, of course, that K_v is locally constant). In the simple case of an axisymmetric vortex, there is no pressure gradient force in the azimuthal direction and so this force does not appear in the leading-order balance given by Equation (14). As in the above assessment of radial Ekman balance, we do not here separate the linear (gradient) and nonlinear (agradient) terms in the vorticity influx term. Inspecting Figure 3a,h, the tangential Ekman balance is reasonably satisfied in the outer vortex boundary layer beyond approximately 100 km radius. However, it is not well satisfied within approximately 70 km radius, especially around the RMW wherein $V_{m\zeta}$ markedly exceeds V_{dz}. Indeed, Figure 3 shows that within approximately 70 km from the vortex centre, all terms, save for horizontal diffusion (V_{dh}) contribute markedly to the mean tangential velocity tendency. In particular, the vertical advection of mean and eddy tangential velocity, V_{mv} and V_{ev}, respectively, make significant contributions to the mean tendency near the RMW in the boundary layer. Therefore, as with the radial Ekman balance, tangential Ekman balance is a poor approximation in the high-wind region of the vortex.

The foregoing results are found to hold true at later times during the intensification process, and the degree of Ekman imbalance is found to increase as the vortex intensifies (not shown). The increased Ekman imbalance can be anticipated by the quadratic nonlinearity of the equations as the vortex strengthens.

In summary, these findings point to the inconsistency of the generalized Ekman balance in the inner-core boundary layer during vortex spin-up and indicate that "explanations" of the flow structure during vortex spin-up that invoke this balance are suspect and should be avoided. These results extend the findings and interpretations of Vogl and Smith (2009), Abarca *et al.* (2015) and Smith and Montgomery (2020) to a period of rapid intensification of a three-dimensional tropical cyclone. These former studies focussed on the mature phase of a tropical cyclone, either during its quasi-steady stage or just prior to and during secondary eyewall formation.

4.5 | Upper-level inflow jets

The existence of the inward agradient force provides a basic explanation for the occurrence of inflow layers that sandwich the upper-tropospheric outflow layer. As pointed out by Wang *et al.* (2020), a way to think about the upper-level outflow layer is to consider it as an expanding jet of air emanating from a mass and radial momentum source where the eyewall convection terminates (Ooyama, 1987). The outward expansion is resisted by a radially inward pressure gradient force (e.g., Smith *et al.*, 2018, figure 5c,d), recalling that the centrifugal force is always positive and the Coriolis force in the radial direction is positive as long as the tangential flow remains cyclonic. Because the induced pressure field extends vertically beyond just the outflow layer itself, one can expect a flow response vertically beyond the outflow layer as well. Where this inward force persists, it will act to accelerate air parcels inwards.

Wang *et al.* (2020) have carried out a more thorough investigation of these inflow jets in a separate study using this framework in which the vertical resolution in their model is increased in the upper troposphere at the expense of that in low levels within the frictional boundary layer. In particular, Wang *et al.* show that interpretations of the inflow jets in terms of axisymmetiric balance dynamics are problematic. They show also that the inflow jets have a significant degree of azimuthal asymmetry.

5 | CONCLUSIONS

We have used an idealized, three-dimensional, 1 km horizontal grid spacing numerical simulation to explore new aspects of vortex spin-up in the framework of the rotating-convection paradigm. As in previous studies, the maximum tangential winds are found to occur within and near the top of the boundary layer, while the maximum radial inflow is at or just above the surface. As the mean vortex intensifies, spin-up in the boundary layer is accompanied by the development of azimuthal-mean supergradient winds that exceed the gradient wind by up

to 20%. Reflecting the strong radial inflow in the boundary layer, the maximum mean tangential wind occurs as much as 10 km inside the maximum gradient wind. The wind asymmetries, associated in part with the asymmetric deep convection, make a substantive contribution (∼30%) to the maximum wind speed inside the radius of this maximum.

As is well known, the boundary-layer dynamics cannot be considered strictly in isolation as they depend on the vortex evolution above the boundary layer, which itself depends on the ability of the convection to amplify the winds above the boundary layer by the classical spin-up mechanism. An improved understanding of the flow within and above the boundary layer is afforded by an analysis of *both* the azimuthal-mean tangential and radial wind tendency equations during vortex spin-up.

As a start, we have extended a previous analysis of the tangential momentum dynamics to a higher spatial resolution and quantified the net effect of convective eddies and the associated waves they generate on the spin-up of the vortex. The analysis shows that the eddies make a substantial contribution to the spin-up of the eyewall region, confirming previous findings.

A particular novelty of the study is an analysis of the mean radial momentum dynamics during the intensification of the vortex. The radial force fields highlight a significant degree of gradient wind imbalance in much of the intensifying inner-core vortex as well as much of the upper troposphere. This analysis points to the important role of gradient wind imbalance in driving the radial circulation within the intensifying vortex. As an illustration of the utility of this dynamical framework, a basic explanation of the inflow layers sandwiching the upper tropospheric outflow layer is obtained from an examination of the inward agradient force per unit mass and the vertical transport of radial momentum by the mean and eddy components of the flow.

In recent years, a generalized Ekman balance approach has been advocated to interpret vortex boundary-layer structure during spin-up and secondary eyewall formation. Our present analysis has shown that generalized Ekman balance is a poor approximation in the inner-core region during vortex spin-up and should not be invoked to "explain" the flow structure of the tropical cyclone boundary layer.

The results of this study support and extend prior work of Zhang *et al.* (2001) and Persing *et al.* (2013) and point to significant limitations of a purely axisymmetric and/or balance description of tropical cyclone intensification.

ACKNOWLEDGEMENTS

ORCID
Michael T. Montgomery https://orcid.org/0000-0001-5383-4648
Gerard Kilroy https://orcid.org/0000-0002-9240-6555
Roger K. Smith https://orcid.org/0000-0002-3668-1608

REFERENCES
Abarca, S.F., Montgomery, M.T. and McWilliams, J.C. (2015) The azimuthally averaged boundary-layer structure of a numerically simulated major hurricane. *Journal of Advances in Modeling Earth Systems*, 7, 1207–1219.

Bryan, G.H. (2002). An investigation of the convective region of numerically simulated squall lines. PhD thesis, Pennsylvania State University, Pennsylvania, PA, USA.

Bryan, G.H. and Fritsch, J.M. (2002) A benchmark simulation for moist non-hydrostatic numerical models. *Monthly Weather Review*, 130, 2917–2928.

Chen, Y., Brunet, G. and Yau, M.K. (2003) Spiral bands in a simulated hurricane. Part II: wave activity diagnosis. *Journal of the Atmospheric Sciences*, 60, 1239–1756.

Črnivec, N., Smith, R.K. and Kilroy, G. (2016) Dependence of tropical cyclone intensification rate on sea surface temperature. *Quarterly Journal of the Royal Meteorological Society*, 142, 1618–1627.

Dunion, J.P. (2011) Rewriting the climatology of the tropical North Atlantic and Caribbean Sea atmosphere. *Journal of Climate*, 24, 893–908.

Emanuel, K.A. (2018) 100 years of progress in tropical cyclone research. *Meteorological Monographs*, 59, 15.1–15.68.

Fang, J. and Zhang, F. (2011) Evolution of multiscale vortices in the development of hurricane *Dolly* (2008). *Journal of the Atmospheric Sciences*, 68, 103–122.

Gill, A.E. (1982) *Atmosphere–Ocean Dynamics*. Academic Press, New York, NY.

Kepert, J.D. (2001) The dynamics of boundary layer jets within the tropical cyclone core. Part I: linear theory. *Journal of the Atmospheric Sciences*, 58, 2469–2484.

Kepert, J.D. (2013) How does the boundary layer contribute to eyewall replacement cycles in axisymmetric tropical cyclones?. *Journal of the Atmospheric Sciences*, 70, 2808–2830.

Kepert, J.D. and Wang, Y. (2001) The dynamics of boundary-layer jets within the tropical cyclone core. Part II: nonlinear enhancement. *Journal of the Atmospheric Sciences*, 58, 2485–2501.

Kilroy, G. and Smith, R.K. (2016) A numerical study of deep convection in tropical cyclones. *Quarterly Journal of the Royal Meteorological Society*, 142, 3138–3151.

Kilroy, G., Smith, R.K. and Montgomery, M.T. (2016) Why do model tropical cyclones grow progressively in size and decay in intensity after reaching maturity? *Journal of the Atmospheric Sciences*, 73, 487–503.

Kilroy, G., Smith, R.K. and Montgomery, M.T. (2017) A unified view of tropical cyclogenesis and intensification. *Quarterly Journal of the Royal Meteorological Society*, 143, 450–462.

Kilroy, G., Smith, R.K. and Montgomery, M.T. (2018) The role of heating and cooling associated with ice processes on tropical cyclogenesis and intensification. *Quarterly Journal of the Royal Meteorological Society*, 144, 99–114.

Landau, L.D. and Lifshitz, E.M. (1966) *Fluid Mechanics* (3rd ed.) Pergamon Press, Oxford, UK.

Mapes, B.E. and Zuidema, P. (1996) Radiative dynamical consequences of dry tongues in the tropical troposphere. *Journal of the Atmospheric Sciences*, 53, 620–638.

Montgomery, M.T. and Smith, R.K. (2014) Paradigms for tropical cyclone intensification. *Australian Meteorological and Oceanographic Journal*, 64, 37–66.

Montgomery, M.T. and Smith, R.K. (2017) Recent developments in the fluid dynamics of tropical cyclones. *Annual Review of Fluid Mechanics*, 49, 541–574.

Montgomery, M.T., Nichols, N.E., Cram, T.A. and Saunders, A.B. (2006) A vortical hot tower route to tropical cyclogenesis. *Journal of the Atmospheric Sciences*, 63, 355–386.

Nguyen, V.S., Smith, R.K. and Montgomery, M.T. (2008) Tropical-cyclone intensification and predictability in three dimensions. *Quarterly Journal of the Royal Meteorological Society*, 134, 563–582.

Ohno, T. and Satoh, M. (2015) On the warm core of a tropical cyclone formed near the tropopause. *Journal of the Atmospheric Sciences*, 72, 551–571.

Ooyama, K.V. (1987). Numerical experiments of steady and transient jets with a simple model of the hurricane outflow layer. Extended abstract pp. 318–320 in 17th Conference on Hurricanes and Tropical Meteorology, Miami, FL. American Meteorological Society, Boston, MA.

Penny, A.B., Harr, P.A. and Doyle, J.D. (2016) Sensitivity to the representation of microphysical processes in numerical simulations during tropical storm formation. *Monthly Weather Review*, 144, 3611–3630.

Persing, J., Montgomery, M.T., McWilliams, J. and Smith, R.K. (2013) Asymmetric and axisymmetric dynamics of tropical cyclones. *Atmospheric Chemistry and Physics*, 13, 12249–12341.

Reasor, P.D. and Montgomery, M.T. (2015) Evaluation of a heuristic model for tropical cyclone resilience. *Journal of the Atmospheric Sciences*, 72, 1765–1782.

Smith, R.K. (2006) Accurate determination of a balanced axisymmetric vortex in a compressible atmosphere. *Tellus*, 58A, 98–103.

Smith, R.K. and Montgomery, M.T. (2016) Understanding hurricanes. *Weather*, 71, 219–223.

Smith, R.K. and Montgomery, M.T. (2020) The generalized Ekman model for the tropical cyclone boundary layer revisited: the myth of inertial stability as a restoring force. *Quarterly Journal of the Royal Meteorological Society*. in press.

Smith, R.K., Montgomery, M.T. and Vogl, S. (2008) A critique of Emanuel's hurricane model and potential intensity theory. *Quarterly Journal of the Royal Meteorological Society*, 134, 551–561.

Smith, R.K., Montgomery, M.T. and Nguyen, S.V. (2009) Tropical cyclone spin-up revisited. *Quarterly Journal of the Royal Meteorological Society*, 135, 1321–1335.

Smith, R.K., Montgomery, M.T. and Kilroy, G. (2018) The generation of kinetic energy in tropical cyclones revisited. *Quarterly Journal of the Royal Meteorological Society*, 145, 2481–2490.

Vogl, S. and Smith, R.K. (2009) Limitations of a linear model for the hurricane boundary layer. *Quarterly Journal of the Royal Meteorological Society*, 135, 839–850.

Wang, S., Smith, R.K. and Montgomery, M.T. (2020) Upper-tropospheric inflow layers in tropical cyclones. *Quarterly Journal of the Royal Meteorological Society*. in press.

Zhang, D.L., Liu, Y. and Yau, M.K. (2001) A multi-scale numerical study of hurricane *Andrew* (1992). Part IV: unbalanced flows. *Monthly Weather Review*, 61, 92–107.

Zhang, J.A. and Montgomery, M.T. (2012) Observational estimates of the horizontal eddy diffusivity and mixing length in the low-level region of intense hurricanes. *Journal of the Atmospheric Sciences*, 69, 1306–1316.

Zhang, J.A., Rogers, R.F., Nolan, D.S. and Marks, F.D. Jr. (2011) On the characteristic height scales of the hurricane boundary layer. *Monthly Weather Review*, 139, 2523–2535.